

Multiscale modeling of dislocation-mediated plasticity of refractory high entropy alloys

Feng Zhao ^{a,b}, Wenbin Liu ^a, Xin Yi ^a, Yin Zhang ^{a,*}, Huiling Duan ^{a,b,*}

^a State Key Laboratory for Turbulence and Complex Systems, Department of Mechanics and Engineering Science, BIC-ESAT, College of Engineering, Peking University, Beijing 100871, China

^b HEDPS, CAPT and IFSA, Collaborative Innovation Center of MoE, Peking University, Beijing 100871, China



ARTICLE INFO

Keywords:

Refractory high entropy alloys
Kink-pair nucleation
Kink migration
Nudged elastic band method
Multiscale simulations

ABSTRACT

Refractory high entropy alloys (RHEAs) have drawn growing attention due to their remarkable strength retention at high temperatures. Understanding dislocation mobility is vital for optimizing high-temperature properties and ambient temperature ductility of RHEAs. Nevertheless, fundamental questions persist regarding the variability of dislocation motion in the rugged energy landscape and the effective activation barrier for specific mechanisms, such as kink-pair nucleation and kink migration. Here we perform systematic atomistic simulations and conduct statistical analysis to obtain the effective activation barriers for the mechanisms underlying various types of dislocation motion in a typical RHEA, NbMoTaW. Moreover, a stochastic line tension model is developed to calculate the activation barrier with substantially reduced computational costs. By incorporating the effective activation barriers into the crystal plasticity model, a multiscale simulation framework for predicting the mechanical properties of RHEAs is established. The ambient temperature yield strength of NbMoTaW is well-predicted by the kink-pair nucleation mechanism of screw dislocations, while the strengthening originating from screw dislocations does not predominate at high temperatures. Our work provides a robust foundation for atomistic studies of effective dislocation behaviors in random solution solids, elucidating the intricate relationship between microscopic mechanisms and macroscopic properties.

1. Introduction

High entropy alloys (HEAs) characterized by composition fluctuations have gained significant interest in recent years, due to their exceptional combination of properties that are rarely accomplished in other metallic materials (George et al., 2019; Li et al., 2021; Tsai and Yeh, 2014; Zhang et al., 2014). Currently, there are two main kinds of HEAs reported in the literature. The first kind is based on 3d transition elements such as Fe, Co, Cr, Ni and Cu, exhibiting a face-centered cubic (FCC) structure, which has been extensively studied (Ding et al., 2019; Li et al., 2019). The second kind mainly consists of refractory elements such as Nb, Mo, Ta, V and W, adopting a body-centered cubic (BCC) phase (Senkov et al., 2018), often referred to as the refractory high entropy alloys (RHEAs). RHEAs have been attracting growing attention since 2010 (Senkov et al., 2010) for their remarkable strength retention at high temperatures (Hu et al., 2021; Senkov et al., 2011), though the low ductility at ambient temperature still limits their formability and application (Mak

* Corresponding authors at: State Key Laboratory for Turbulence and Complex Systems, Department of Mechanics and Engineering Science, BIC-ESAT, College of Engineering, Peking University, Beijing 100871, China.

E-mail addresses: yinzhang@pku.edu.cn (Y. Zhang), hlduan@pku.edu.cn (H. Duan).

et al., 2021; Tandoc et al., 2023; Zhang et al., 2023). While existing investigations are mostly experimental studies focusing on the processing and macroscopic mechanical behaviors of RHEAs (Coury et al., 2019; Xiong et al., 2023), there is a growing recognition of the need for simulations and theoretical studies (Zhou et al., 2023), which are essential for comprehending the microscopic mechanisms with chemical fluctuations, aspects not easily accessible through experimental methods.

Understanding the mobility of dislocations is crucial to achieving both high-temperature properties (Wang et al., 2020; Zhou et al., 2023) and ambient temperature ductility (Mak et al., 2021; Qi and Chrzan, 2014) in RHEAs. It has been established in pure BCC metals and dilute alloys that screw dislocations are much harder to move, and thus play a crucial role in controlling plastic deformation (Seeger, 1995, 2001; Seeger and Holzwarth, 2006). However, recent molecular dynamics (MD) simulations have revealed that the mobility discrepancy between screw and edge dislocations is narrowed in RHEAs (Chen et al., 2023, 2020a; Yin et al., 2021). The edge dislocations may have lower mobility and control plastic deformation at high temperatures (He et al., 2023; Kubilay et al., 2021; Lee et al., 2021; Li et al., 2020a). The sluggish motion of edge dislocations is consistent with experimental observations (Lee et al., 2020, 2021; Wang et al., 2020). However, conventional MD simulations encounter two major challenges when investigating dislocation behaviors in RHEAs. Firstly, the high strain rate of MD simulations often lacks relevance to the thermal activation regime of dislocation motion typical for quasi-static loading (Fan et al., 2013; Gurrutxaga-Lerma et al., 2020). Secondly, these works mentioned above have primarily focused on limited examples of dislocation motion due to time and computational costs. While informative, these studies struggle to provide a comprehensive understanding of the variability in dislocation behaviors due to the inherently variable local chemical environment of HEAs. Extracting effective activation barriers for individual mechanisms calls for statistically significant data and robust statistical analysis (Fey et al., 2022). In addition, despite the extensive attention on the dominant role of edge dislocations at high temperatures (He et al., 2023; Kubilay et al., 2021; Lee et al., 2021; Li et al., 2020a), the behavior of screw dislocations in REAHs is comparatively less explored. Nevertheless, recognizing the significance of screw dislocations is vital in constructing a whole picture of solution strengthening in RHEAs, and is relevant to the ambient-temperature ductility problem (Chen et al., 2020b; Li et al., 2020b; Mak et al., 2021; Senkov et al., 2021).

Therefore, a systematic investigation of dislocation behavior with randomness in RHEAs becomes imperative. This entails conducting thorough atomistic calculations and subsequently conducting statistical analysis of the obtained data. The nudged elastic band (NEB) method is advantageous in capturing the reaction pathways and activation barriers of thermally activated, stress-driven processes (Zhang et al., 2022; Zhu et al., 2013). Despite its application in determining the reaction pathway of dislocation motion in RHEAs, only a few cases have been demonstrated (Wang et al., 2022). Furthermore, the presence of significant chemical fluctuations complicates the acquisition of effective dislocation properties for integration into broader-scale simulations. Although the NEB method allows for a direct atomistic determination of the saddle-point configurations and activation barriers of kink-pair nucleation, it still suffers from high computational costs. A line tension model initially proposed by Dezerald et al. (2015) has been used to study kink-pair nucleation in pure BCC metals. This model enables the determination of the kink-pair nucleation barrier, but it has not been extended to BCC alloys or the specific situation in RHEAs.

So far, simulations and theoretical studies on RHEAs focus on revealing the microscale deformation mechanisms, whereas the plastic deformation of RHEAs contains complicated interactions coupled across various scales. This scale-coupling calls for multiscale frameworks to effectively unravel the mechanical behavior. Mechanical properties of RHEAs have been studied by incorporating MD, dislocation dynamics, and crystal plasticity simulations (Cereceda et al., 2016; Fang et al., 2022; Kumar et al., 2023; Lin et al., 2022; Po et al., 2016). Due to the high strain rate and limited time scale, MD is unable to sample the thermally activated processes at quasi-static loading conditions or to capture the activation barrier of kink-pair nucleation and kink migration. With the ability to properly capture thermally activated processes, the NEB method has been incorporated into the crystal plasticity model to form a multiscale framework

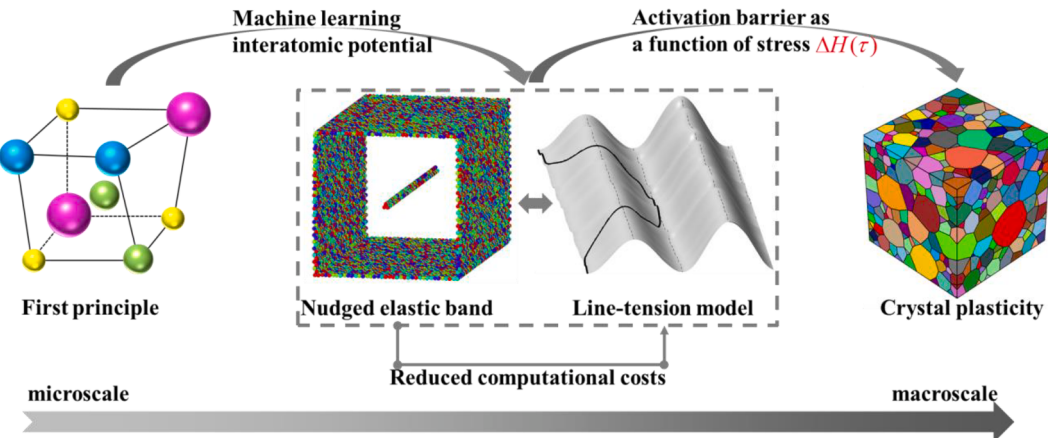


Fig. 1. Schematic of the multiscale simulation framework. The accuracy of the first-principle simulations is conveyed to the NEB simulations through a machine learning interatomic potential (Yin et al., 2021). A stochastic line tension model is developed to obtain the activation barrier of kink-pair nucleation with substantially reduced computational costs. The obtained activation barrier, as a function of shear stress, is then incorporated into crystal plasticity simulations to determine the stress-strain relationship of polycrystalline NbMoTaW.

(Narayanan et al., 2014).

In this work, we perform systematic NEB calculations on a typical RHEA, NbMoTaW, and conduct statistical analysis to determine the effective activation barrier of kink-pair nucleation in Section 2. A stochastic line tension model considering the distribution of Peierls barriers is developed in Section 3, which provides activation barriers in agreement with NEB results. Section 4 incorporates the effective energy barriers from the statistical analysis of NEB calculations into the crystal plasticity model, allowing the derivation of the stress-strain relationship and temperature-dependent yield strength for NbMoTaW. The overall multiscale simulation framework utilized in this study, which integrates the NEB method and the crystal plasticity model, is illustrated in Fig. 1. Some discussions are presented in Section 5, followed by conclusions in Section 6.

2. NEB simulations of screw dislocations

Here we employ three-dimensional (3D) NEB simulations to study the screw dislocation glide in RHEAs, characterized by a rugged energy landscape (Wang et al., 2020). According to the transition state theory (Phillips, 2001; Vineyard, 1957; Wang and Cai, 2023), the rate of dislocation overcoming a barrier with activation Gibbs free energy ΔG is

$$v = v_0 \exp\left(-\frac{\Delta G(\tau, T)}{k_B T}\right), \quad (1)$$

where v_0 is the trial frequency on the order of 10^{11} s^{-1} , k_B is the Boltzmann constant, and T is the temperature. For a typical activation rate of 10^{-3} s^{-1} , ΔG of a dislocation glide process is approximately $30 k_B T$, equivalent to 0.7 eV at room temperature. The temperature-independent part of ΔG , denoted as ΔH , can be obtained from the potential energy surface of an atomic system at 0 K using the NEB method. Since a single dislocation glide can be influenced by the local element ordering, NEB calculations are performed on numerous random configurations. Various ways for extracting the overall behavior of dislocation motion from these calculations are compared. The details are described below.

2.1. Atomistic modeling

As shown in Fig. 2, a screw dislocation is embedded in the simulation supercell by imposing a displacement field according to the elastic solution of a screw dislocation and then relaxing the supercell using the conjugate gradient method. The supercell dimensions are $10 \text{ nm} \times 27 \text{ nm} \times 7 \text{ nm}$ in the $x//[111]$, $y//[\bar{1}01]$, and $z//[\bar{1}2\bar{1}]$ directions, containing 48,600 atoms with an equal number of Nb, Mo, Ta and W atoms. For computational efficiency, a dislocation length of $36b$ is adopted with b as the size of Burgers vector ($\%<111>$). With this dislocation length, the screw dislocation segment undergoes kink-pair nucleation and kink migration, while shorter segments propagate as a straight line. Periodic boundary conditions are imposed in the x - and z -directions. Through performing NEB simulations on pure metal Mo with different dislocation lengths, it is observed that the effect of the attraction between two kinks across the periodic boundary is insignificant. Additionally, the dimensions in the y - and z -directions are also tested to ensure that the size of the supercell has negligible influence on the outcomes of the simulations. The centrosymmetry parameter (Kelchner et al., 1998) is employed to filter out crystal defects, and thus the upper and lower free surface layers are shown along with the dislocation line. The left and right boundaries are not shown because the periodic boundary conditions are imposed.

Fig. 2(a) shows the initial state of the screw dislocation in the middle of the simulation supercell. The loading scheme for the stress-controlled NEB method (Si et al., 2023) is presented in Fig. 2(b). To implement the stress-controlled NEB, a fixed force f_x is imposed on each atom in the top two y -surfaces, and an opposite force $-f_x$ is applied to each atom in the bottom two y -surfaces. The resulting shear stress is $\tau = (N \times f_x) / (L_x \times L_z)$, where N is the number of atoms in the top or bottom layer, and L_x and L_z are the lengths of the supercell in the x - and z -directions, respectively. During the simulation, the work done by the fixed forces is added to the potential energy of the system, and this is why the enthalpy change ΔH is used to denote the activation barrier, instead of the energy change ΔE . The final state is established by applying shear stresses discussed above, which moves the dislocation to the adjacent Peierls valley in the negative

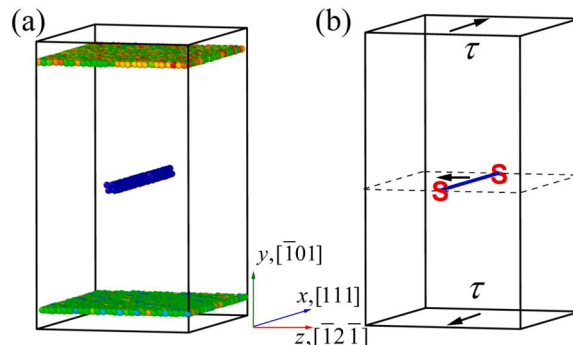


Fig. 2. Atomistic simulation setup. (a) Simulation supercell and the dislocation in its initial energy minimum state, colored by the centrosymmetry parameter (Stukowski, 2010). (b) Schematic of the supercell showing the specifics of the loading scheme.

z -direction, followed by energy minimization using the conjugate gradient method. The stress-controlled NEB method (Si et al., 2023) is carried out using the parallel molecular dynamics simulator LAMMPS (Thompson et al., 2022). 42 replicas are generated via a linear interpolation between the initial and final states, with an inter-replica nudging force connecting neighboring replicas. The stopping tolerance for force is set at 0.005 eV/Å. Simulation results are visualized using OVITO (Stukowski, 2010).

Machine learning potentials (MLPs) have been developed to transfer the accuracy of quantum mechanical methods to atomistic simulations (Hu et al., 2019; Wang et al., 2021; Zheng et al., 2023). A state-of-the-art machine learning interatomic potential known as the moment tensor potential (MTP) is employed here (Yin et al., 2021). The accuracy of the interatomic potential is verified in Yin et al. (2021) regarding the basic properties such as melting points, unstable stacking fault energy and elastic constants. The dislocation core structure is characterized using a differential displacement map, a technique pioneered by Vitek et al. (1970). To verify this interatomic potential, the differential displacement plots of the screw dislocation cores of Nb, Mo, Ta, and W predicted by the MTP are displayed in Fig. 3. In the plot, white, grey, and black colors denote atoms on three different (111) faces, while black arrows indicate the differential displacement vectors. The lengths of these vectors are proportional to the relative displacement of neighboring atoms from a perfect crystal configuration to a defect configuration. Dislocation cores of the four pure metals are all non-degenerate, symmetrically spread in the three (110) planes perpendicular to the [111] direction. This core structure is compatible with *ab initio* simulation results (Rodney et al., 2017; Shimizu et al., 2007), and supports stabilized glide on a (110) plane, consistent with experimental data (Chaussidon et al., 2006). In contrast, atomistic simulations with asymmetry degenerate cores predict (112) glide planes, which is less reliable than the results with non-degenerate cores (Chaussidon et al., 2006).

At each applied load, a total of 600 three-dimensional (3D) NEB calculations of screw dislocation glide are performed. The arrangement of elements is shuffled before each calculation. Fig. 4 depicts the representative minimum energy path (MEP) and dislocation configurations at zero stress. The enthalpy H of the final state is about 0.3 eV higher than that of the initial state due to the difference in local element ordering. The red dots in Fig. 4 represent the local enthalpy maximum along the MEP, with corresponding dislocation configurations shown in Fig. 4(b)-(f). The first activation barrier (Fig. 4(b)) is related to a kink-pair nucleation event, while the second and third barriers are related to the migration of the right kink, and the fourth and fifth barriers are related to the migration of the left kink. The activation barrier for kink-pair nucleation is 0.7 eV, and the activation barrier for kink migration is about 0.1 eV to 0.2 eV. Compared to pure BCC metals (Narayanan et al., 2014), RHEAs exhibit a relatively higher activation barrier of kink migration. Nevertheless, kink-pair nucleation continues to play a substantial role. Note that the dislocation lines often exhibit a curved shape in MD simulations (Yin et al., 2021), whereas in this study, we primarily aim to clarify the activation barriers of kink-pair nucleation and kink migration considering the effect of the local atomic configuration. Therefore, a local unit process is considered featuring a single nucleation event, so that the dislocation segment remains relatively straight.

The shear stress-dependent MEPs of three randomly selected calculations out of 600 are presented in Fig. 5(a)-(c). The slopes of the MEPs decrease with increasing applied stress, leading to a corresponding reduction in the barrier energy. Analyzing the MEPs for shear stresses ranging from 50 MPa to 1000 MPa indicates that the small barriers under low stress gradually diminish and almost vanish at 1000 MPa. The remaining barrier under high shear stress is related to kink-pair nucleation. For each applied load, the average MEP of 600 calculations is displayed in Fig. 5(d), with the shaded regions representing the error bands, illustrating the influence of the inherently variable local chemical environment.

To confirm the relative importance of kink-pair nucleation and kink migration, we extract the activation barriers from all 600 calculations for each applied stress, including both kink-pair nucleation and kink migration, and perform a statistical analysis. Fig. 5(e)-(f) presents the probability distribution of activation barrier under 50 MPa and 500 MPa. The profile shows two distinct regions of high and low energy levels, fitting well with the superposition of two Weibull distributions.

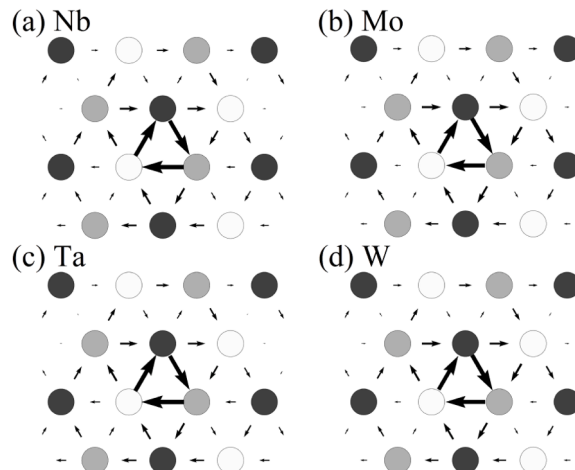


Fig. 3. Differential displacement plot illustrating the non-degenerate screw dislocation core of Nb, Mo, Ta, and W predicted using the moment tensor potential (MTP) (Yin et al., 2021).

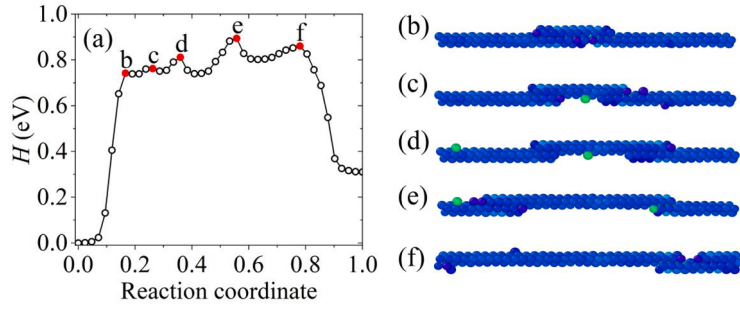


Fig. 4. (a) NEB results of screw dislocation glide without applied loading. (b)-(f) Panels correspond, respectively, to the dislocation configurations at five local saddle points in (a), colored using the centrosymmetry parameter (Stukowski, 2010). The first saddle point corresponds to kink-pair nucleation and the rest are kink migration.

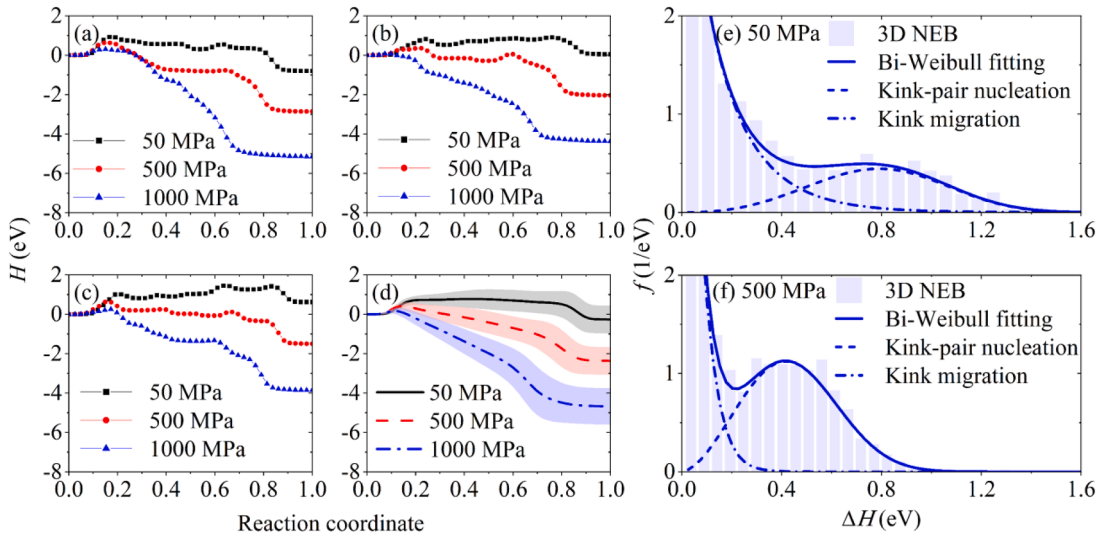


Fig. 5. Shear stress-dependent MEPs for screw dislocation glide using the NEB method and statistical analysis of the activation barrier. Three randomly selected calculations out of 600 are depicted in (a)-(c), corresponding to MEPs of different configurations with random atom arrangements. The average MEPs are shown in (d) with accompanying error bands. The probability distribution f of activation barrier ΔH involving both kink-pair nucleation and kink migration under shear stress of (e) 50 MPa and (f) 500 MPa.

$$f(\Delta H, c_1, \lambda_1, c_2, \lambda_2, A) = Af_1(c_1, \lambda_1) + (1 - A)f_2(c_2, \lambda_2), \quad (2)$$

where

$$f_i(\Delta H, c_i, \lambda_i) = \frac{c_i}{\lambda_i} \left(\frac{\Delta H}{\lambda_i} \right)^{c_i-1} \exp \left[- \left(\frac{\Delta H}{\lambda_i} \right)^{c_i} \right], \quad i = 1, 2. \quad (3)$$

The parameters c_i and λ_i are the shape and scale parameters, respectively, ΔH denotes the activation enthalpy, and A is the mixing weight of the first Weibull distribution f_1 . Note that this distribution depends on the dislocation length. A longer dislocation segment could have a lower activation enthalpy due to the higher likelihood of exploring atomic distributions that are favorable for activation along the dislocation line. The high-energy region of the probability distribution corresponds to kink-pair nucleation, and the low-energy region corresponds to kink migration. Fig. 5 clearly indicates that kink migration often shows a much lower activation barrier, and this barrier decreases rapidly with the increase in external loading. Note that the application of Weibull distribution is rationalized by the extreme value distribution theory (Kotz and Nadarajah, 2000). Suppose that multiple possible nucleation sites exist on the dislocation line with nucleation barriers $\Delta H^1, \dots, \Delta H^n$, which are random samples from the same distribution. The actual barrier calculated is the minimal one. According to the extreme value distribution theory, if $\min\{\Delta H^1, \dots, \Delta H^n\}$ or its linear transformation tends to a limit, the limit can only be one of three types (Kotz and Nadarajah, 2000), and one of these types is the Weibull distribution. In short words, mathematically, the Weibull distribution naturally arises from the extreme value distribution theory. It has also been utilized by Weibull in describing the distribution of the strength of brittle materials (Weibull, 1939).

As shown in Fig. 5(e)-(f), kink-pair nucleation may be more critical in determining the mechanical behavior of the NbMoTaW alloy,

\Delta H are depicted against the enthalpy difference between the initial state and the final state ΔH_{final} . The correlation coefficient is defined as $r(\Delta H, \Delta H_{\text{final}}) = \text{cov}(\Delta H, \Delta H_{\text{final}})/(\sigma_{\Delta H}\sigma_{\Delta H_{\text{final}}})$, where $\text{cov}(\Delta H, \Delta H_{\text{final}})$ is the covariance and σ denotes the standard error. The scatter plots of 50 MPa and 500 MPa show a linear relationship with the correlation coefficients of 0.59 and 0.58, respectively. Also, by plotting the value of the slope against the stress (not shown here), one can find that the slope decreases linearly with increasing shear stress. Note that a similar linear correlation is identified for cross-slip barrier and energy difference in FCC alloys such as Ni-Al and Cu-Ni (Nöhring and Curtin, 2017).

2.2. Effective activation enthalpy

Each of the 3D NEB calculations described above can be regarded as a unit process, representing a segment of screw dislocation moving by a small distance equivalent to the spacing between neighboring Peierls valleys. To obtain the overall stress-driven thermally activated dislocation behavior, which can be connected to the macroscale mechanical properties, the calculation results need to be averaged. As discussed above, only the barriers related to kink-pair nucleation are considered here. Three averaging methods are utilized and compared below.

The first averaging method is a simple arithmetic mean $\Delta H_{\text{eff}} = \sum_j \Delta H_j / N$, where ΔH_j is the activation barrier of kink-pair nucleation from the j -th calculation, and N is the total number of activation barrier data. However, this approach lacks physical meaning.

The second averaging method is termed waiting-time averaging. Similar to Eq. (1), the activation rate v_j of each unit process is expressed as $v_j = v_0 \exp(-\Delta H_j / k_B T)$, and the reciprocal of the activation rate v_j gives the waiting time required for the dislocation segment to overcome the activation barrier, denoted as $t_j = 1/v_j$. Following the kink-pair nucleation event, the dislocation segment can propagate a distance equivalent to the spacing between neighboring Peierls valleys, L_p . The velocity of the segment V_j is expressed as $V_j = L_p/t_j = v_j L_p$. Supposing that the process of one dislocation segment continuously propagating multiple Peierls valleys in the forward direction can be approximated by the arrangement of all individual NEB calculations, the average dislocation velocity V_{eff} is given by $V_{\text{eff}} = N L_p / \sum_j t_j$, which is also related to the effective activation rate v_{eff} by $V_{\text{eff}} = v_{\text{eff}} L_p$. Therefore, the effective activation rate is obtained as

$$v_{\text{eff}} = \frac{N}{\sum_j t_j} = \frac{v_0 N}{\sum_j \exp(\Delta H_j / k_B T)}. \quad (4)$$

By taking the logarithm of both sides of Eq. (1), the effective activation barrier can be related to the effective activation rate by

$$\Delta H_{\text{eff}}(\tau) = -\frac{d(\ln v_{\text{eff}})}{d\left(\frac{1}{k_B T}\right)}. \quad (5)$$

Substituting Eq. (4) into Eq. (5), the effective activation barrier by the waiting-time averaging is expressed as (Labusch, 1988)

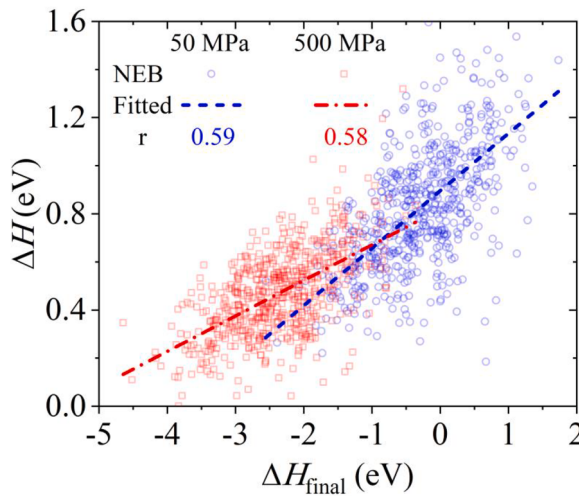


Fig. 6. Correlation between the activation barrier ΔH and enthalpy difference ΔH_{final} under shear stress of 50 MPa and 500 MPa, showing a linear relationship with correlation coefficient 0.59 and 0.58, respectively.

$$\Delta H_{\text{eff}} = \frac{\sum_j \Delta H_j \exp(\Delta H_j / k_B T)}{\sum_j \exp(\Delta H_j / k_B T)}. \quad (6)$$

As discussed above, ΔH follows the Weibull distribution as $\Delta H \sim \text{Weibull}(c, \lambda)$. The probability density function of activation barrier is $f(\Delta H)$, and Eq. (6) can be written in a continuous form as

$$\Delta H_{\text{eff}} = \frac{\int_0^{+\infty} \Delta H f(\Delta H) \cdot e^{\frac{\Delta H}{kT}} d\Delta H}{\int_0^{+\infty} f(\Delta H) e^{\frac{\Delta H}{kT}} d\Delta H}. \quad (7)$$

The waiting-time averaging is a weighted averaging with the weight parameter in exponential form. When the temperature is not too high, the original waiting time averaging (Eq. (6)) is close to an extreme value, where the overall activation barrier is determined by the strongest barrier. This may be applicable along the forward direction of dislocation, since the dislocation must overcome all the barriers ahead to generate plastic flow. However, along the dislocation line, the kink-pair may nucleate at the most favorable location, representing the “weakest link”. In essence, both mechanisms may work simultaneously.

Therefore, we propose a two-level averaging method involving minimization along the dislocation line (x -direction in Fig. 2) and waiting-time averaging along the forward direction (negative z -direction in Fig. 2). The process of the two-level averaging method is as follows. First, the NEB calculations are randomly grouped, where the results in the same group are taken to be on the same extended dislocation segment, and the actual activation barrier of kink-pair nucleation along this extended dislocation segment is the minimal one within the group. Different groups represent the dislocations at different positions along the dislocation forward direction, and the overall activation barrier is regulated by the waiting-time averaging. The discrete form of two-level averaging is expressed as

$$\Delta H_{\text{eff}} = \frac{\sum_j \min_i \{\Delta H_{ji}\} \exp(\min_i \{\Delta H_{ji}\} / kT)}{\sum_j \exp(\min_i \{\Delta H_{ji}\} / kT)}, \quad (8)$$

where ΔH_{ji} denotes the i th barrier among the j -th group, and $\min_i \{\Delta H_{ji}\}$ represents the minimization within the j -th group.

Furthermore, describing the distribution of activation barriers using the Weibull distribution, a continuous version of the above process can be obtained. The minimum value of n independent Weibull random variables $\min\{\Delta H_1, \dots, \Delta H_n\}$ has the same distribution as $n^{-1/c} \Delta H$ (Kotz and Nadarajah, 2000), i.e., $\min\{\Delta H_1, \dots, \Delta H_n\} \sim \text{Weibull}(c, n^{-1/c} \lambda)$, where c and λ are the shape and scale parameters, respectively. Then, the waiting-time averaging Eq. (7) is applied to this distribution to obtain the two-level averaging expressed as

$$\Delta H_{\text{eff}} = \frac{\int_0^{+\infty} \Delta H f_n(\Delta H) \cdot e^{\frac{\Delta H}{kT}} d\Delta H}{\int_0^{+\infty} f_n(\Delta H) e^{\frac{\Delta H}{kT}} d\Delta H}, \quad (9)$$

where $f_n(\Delta H)$ is the probability density function of $\min\{\Delta H_1, \dots, \Delta H_n\}$.

Fig. 7 shows the effects of dislocation segment length and temperature on activation barrier calculated using Eq. (9). Since the dislocation length employed in NEB simulations is 10 nm (Fig. 2(a)), the length of the extended dislocation in the two-level averaging is $10 \times n$ nm. At 300 K, the activation barrier decreases as the dislocation length increases (Fig. 7(a)). With dislocation length 50 nm, Fig. 7(b) depicts the temperature effect on the activation barrier. From 300 K to 700 K, the increasing temperature only lowers the activation barrier slightly. Note that the activation volume stays stable across different dislocation lengths and temperatures, indicating that our model effectively captures the essential mechanism.

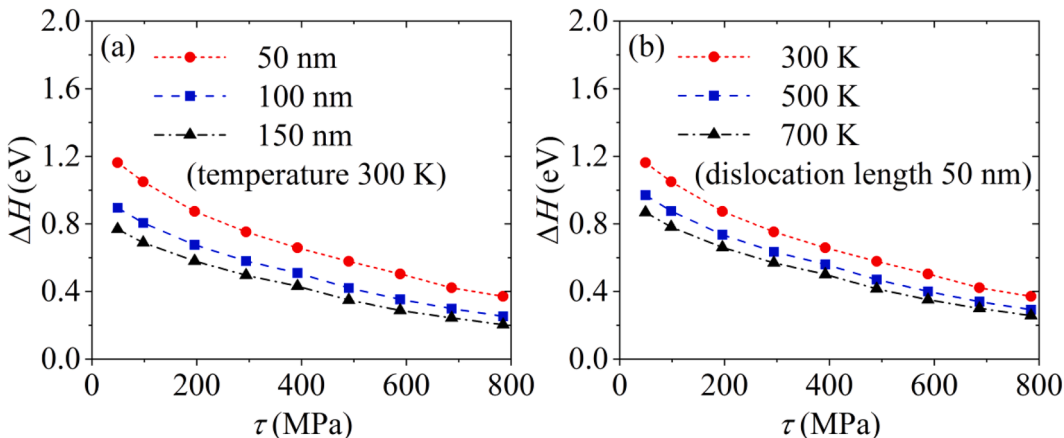


Fig. 7. Effects of (a) dislocation segment length and (b) temperature on activation barrier based on two-level averaging, first choosing the ‘weakest link’ along the dislocation and then applying waiting-time averaging.

Fig. 8 displays a comparison analysis of these three averaging methods. The temperature used in both the waiting-time averaging and the two-level averaging methods is 300 K, and the dislocation length used in the two-level averaging method is 50 nm. The waiting-time averaging gives a zero-stress activation barrier exceeding 2 eV, leading to an overestimation of the yield strength compared to the experimental measurements of NbMoTaW (Senkov et al., 2011). While the simple averaging method and the two-level averaging method give more reasonable results, the former lacks clear physical significance. Hence, the result of the two-level averaging method will be utilized in the subsequent crystal plasticity model in [Section 4](#). Despite methodological differences, the activation volumes given by all three averaging methods are quite close, about $7.6b^3$, since kink-pair nucleation is the rate-limiting mechanism (Narayanan et al., 2014).

3. Stochastic line tension model

As discussed in the previous section, the exploration of screw dislocation kinetics requires a substantial number of 3D NEB calculations, which are time-consuming, especially when using precise machine learning interatomic potentials. In this section, we propose a solution by utilizing a stochastic line tension model, which provides the activation barrier of kink-pair nucleation through the utilization of only two-dimensional (2D) NEB results. This approach offers a substantial reduction in computational resources. The details are as follows.

3.1. Line tension model

In the line tension model, the dislocation line is idealized as a one-dimensional curve represented by a function $z(x)$, as illustrated in **Fig. 9**. The enthalpy of the dislocation comprises contributions from the Peierls barrier, line tension energy and the work done by external loading as (Dezerald et al., 2015; Kang et al., 2012; Rodney and Proville, 2009)

$$H(z, \tau_{xy}) = \int \left[F(z(x)) + \frac{\Gamma}{2} \left(\frac{dz}{dx} \right)^2 - \tau b z(x) \right] dx, \quad (10)$$

where F is the Peierls barrier, Γ is the line tension, τ is the resolved shear stress shown in **Fig. 2(b)**. To connect with atomic simulations, the dislocation is discretized into segments of length b . The normalized z -coordinate of each segment is $Z_n = z_n/L_p$, where z_n is the z -direction coordinate of the n -th segment. Once discretized, the enthalpy is expressed as

$$H(\{Z_n\}, \tau_{xy}) = \sum_n \left[F(Z_n) + \frac{\Gamma L_p^2}{2b} (Z_{n+1} - Z_n)^2 - \tau b^2 L_p Z_n \right]. \quad (11)$$

The activation barrier of kink-pair nucleation and the corresponding dislocation configuration can then be obtained by locating the saddle point of the above enthalpy $H(\{Z_n\}, \tau)$.

The Peierls barrier is assumed to have a cosine shape as

$$F(Z_n) = \frac{\Delta U_n}{2} [1 - \cos(2\pi Z_n)], \quad (12)$$

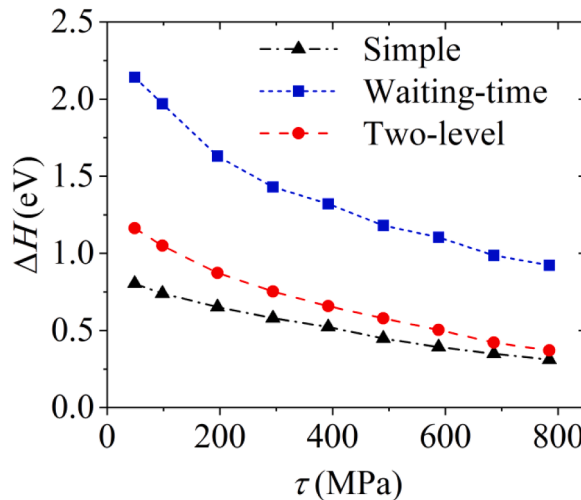


Fig. 8. Comparison of three averaging methods. The temperature used in both the waiting-time averaging and the two-level averaging methods is 300 K, and the dislocation length used in the two-level averaging method is 50 nm.

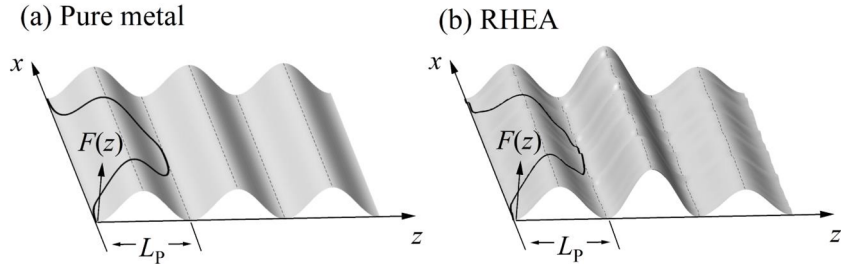


Fig. 9. Schematic of the energy landscape of (a) pure BCC metal and (b) RHEA. The energy landscape of RHEAs is more rugged. F denotes the Peierls barrier, and L_p is the distance between adjacent Peierls valleys.

where ΔU_n is the Peierls barrier varying between dislocation segments. Note that in the model for pure metals, ΔU_n is a constant; while for high-entropy alloys, the probability distribution of ΔU_n can be extracted from 2D NEB calculations, a topic to be discussed in the next section.

3.2. Nudged elastic band simulation of Peierls barrier

The simulation supercell setup for 2D NEB calculations is similar to that for 3D NEB. The dislocation length in 2D NEB ranges from 1b to 9b. Fig. 10 shows the MEP of a calculation with dislocation length 6b moving along the z-negative direction over two Peierls barriers. The reaction coordinates Z are not taken directly from NEB output, but calculated using the following equation to describe the dislocation position (Rodney and Provile, 2009)

$$Z = \frac{1}{b} \left[\sum_{x_j^0 \in Y^+} (x_j - x_j^0) - \sum_{x_j^0 \in Y^-} (x_j - x_j^0) \right], \quad (13)$$

where Y^+ and Y^- denote the two Y planes above and below the dislocation slip plane, and x_j^0 is the x -coordinate of the j -th atom in the initial configuration. The Peierls barriers present an approximate cosine shape with the enthalpy levels at the hills and valleys disturbed by the local element ordering.

A total of 1000 calculations for each dislocation length L are performed at zero applied loading. The activation barrier distribution for a dislocation length of 6b is shown in Fig. 11(a), and the Weibull distribution provides the best fit. Moreover, the relationship between the activation barrier and the enthalpy difference between the initial and final states is analyzed in Fig. 11(b), demonstrating a strong positive correlation with a coefficient of 0.84. Averaging the energy at the same reaction coordinates, an average Peierls barrier of a dislocation length of 6b is obtained in Fig. 11(c). The average barrier aligns well with the expected cosine shape, validating our assumption for function F in the preceding subsection. This cosine shape also works for other dislocation lengths. Taking the standard energy error at the hill points, the relative root-mean-square fluctuation $\sigma_{\Delta H}/\langle \Delta H \rangle$ show a linear relationship with $(L/b)^{-1/2}$ in Fig. 11(d), where $\sigma_{\Delta H}$ is the standard error and $\langle \Delta H \rangle$ is the mean of ΔH . Fig. 11(d) indicates that the fluctuations increase as the dislocation length decreases, while the mean activation barriers for different lengths remain close. Since the dislocation length is proportional to the model particle number, Fig. 11(d) provides intriguing insights in accordance with statistical mechanics. The distribution of the

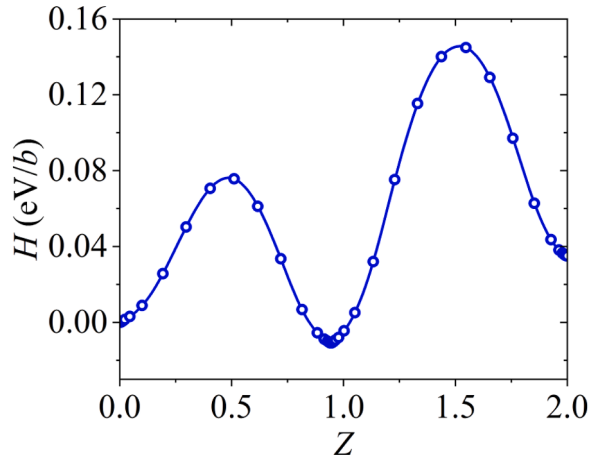


Fig. 10. A representative 2D NEB result of a screw dislocation glide under zero applied loading.

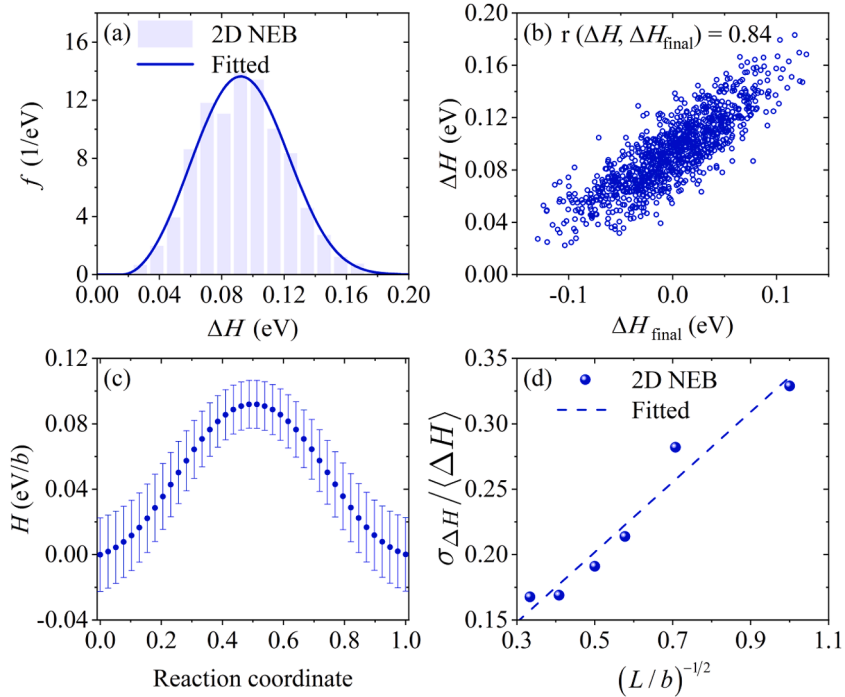


Fig. 11. Statistical analysis of 2D NEB calculations without applied loading. (a) Distribution of activation barriers ΔH . (b) Correlation between activation barrier and enthalpy difference (between the initial and final configurations). (c) Average Peierls barrier of dislocation length $6b$. (d) The relative root-mean-square fluctuation $\sigma_{\Delta H}/\langle \Delta H \rangle$ in the Peierls barrier.

random variable ΔU_n is fitted to the simulation data, yielding a mean of 0.0846 eV and a standard error of 0.0327 eV. The distribution of ΔU_n is then integrated into the stochastic line tension model to determine the saddle point of enthalpy.

3.3. Model results

To obtain an initial configuration sufficiently close to the saddle point, the trial solution for $\{Z_n\}$ is formulated as

$$Z_n = (1 - Z_0) \left\{ \frac{\tanh[\phi(X_n + \varphi)]}{2} - \frac{\tanh[\phi(X_n - \varphi)]}{2} \right\} + Z_0, \quad (14)$$

where X_n is the position for the elementary segments, ranging from $-K$ to K if the dislocation line in the supercell is discretized into $2K + 1$ segments with periodic boundary conditions along the x -direction. Parameters ϕ and φ are yet to be determined, and Z_0 is the dislocation position of the initial state with external loading. To determine the saddle point, the following system of nonlinear equations is solved,

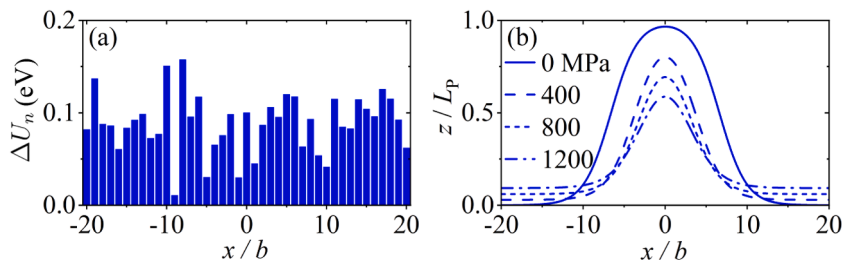


Fig. 12. (a) Peierls barrier ΔU_n attributed to each dislocation segments before solving the nonlinear equation system Eq. (15). (b) Profiles of the dislocation at the saddle point under different shear stresses (0, 400, 800, and 1200 MPa) in one calculation.

$$\begin{cases} \frac{\partial H(\{Z_n\}, \tau)}{\partial \phi} = \sum_n \frac{\partial H(\{Z_n\}, \tau)}{\partial Z_n} \cdot \frac{\partial Z_n}{\partial \phi} = 0, \\ \frac{\partial H(\{Z_n\}, \tau)}{\partial \varphi} = \sum_n \frac{\partial H(\{Z_n\}, \tau)}{\partial Z_n} \cdot \frac{\partial Z_n}{\partial \varphi} = 0. \end{cases} \quad (15)$$

The lattice parameter is 3.22 Å (Maresca and Curtin, 2020) and the line tension Γ is taken as 2.5 eV/Å. The value of K is taken as 20, meaning that the dislocation segment length is $41b$, or 11.4 nm.

A total of 5000 calculations are performed, with a new set of $\{\Delta U_n\}$ sampled from the distribution of ΔU before each calculation. Fig. 12 illustrate the results of one calculation. Fig. 12(a) shows the value of the Peierls barrier ΔU_n attributed to each dislocation segments before solving the nonlinear equation system Eq. (14), and Fig. 12(b) shows the resulting dislocation configurations under external loading. As the shear stress increases, the configuration profiles become more flattened, aligning with the theoretical results of Argon (2008).

Furthermore, to determine the macroscopic effect, we impose a two-level averaging to all calculations. As discussed in Section 2.2, the two-level averaging contains identifying the weakest link along a dislocation length and incorporating it into the waiting-time averaging. The number of dislocation segments in each group is 5, and these 5 segments are taken to be on the same extended dislocation segment, leading to a dislocation length of 57 nm. This is close to the dislocation length used in the averaging of NEB results. The temperature used in the two-level averaging methods is 300 K. As displayed in Fig. 13, the resulting effective activation barrier curve denoted by solid line is in good agreement with the two-level averaging results of 3D NEB calculations denoted by red spheres. Note that for the two-level averaging of 3D NEB calculations, the temperature is also 300 K, and the dislocation length is 50 nm.

4. Atomistically-informed crystal plasticity simulations

Based on the activation barrier of kink-pair nucleation obtained from the microscale simulations, we develop an atomistically-informed crystal plasticity model to describe the macroscale stress-strain responses of NbMoTaW. The constitutive equations are formulated within the rate-dependent, finite-strain framework of elastic-plastic deformation for individual grain (Kalidindi et al., 1992). The deformation gradient of each grain \mathbf{F} is decomposed multiplicatively into the elastic part \mathbf{F}^e and the plastic part \mathbf{F}^p , i.e.,

$$\mathbf{F} = \mathbf{F}^e \cdot \mathbf{F}^p.$$

The time differential of \mathbf{F} is related to the velocity gradient \mathbf{L} by $\dot{\mathbf{L}} = \dot{\mathbf{F}}\mathbf{F}^{-1}$, and the velocity gradient can be further decomposed into two parts, i.e., $\mathbf{L} = \mathbf{L}^e + \mathbf{F}^e \mathbf{L}^p \mathbf{F}^{e-1}$, where $\mathbf{L}^e = \dot{\mathbf{F}}^e \mathbf{F}^{e-1}$ and $\mathbf{L}^p = \dot{\mathbf{F}}^p \mathbf{F}^{p-1}$. The Green strain tensor is related to \mathbf{F}^e as $\mathbf{E}^e = 1/2(\mathbf{F}^{eT} \cdot \mathbf{F}^e - \mathbf{I})$, which can be used to determine the second Piola-Kirchhoff stress tensor \mathbf{T}^* , i.e., $\mathbf{T}^* = \mathbf{C} \cdot \mathbf{E}^e$, where \mathbf{C} is the fourth-order anisotropic elasticity tensor. The plastic velocity gradient \mathbf{L}^p involves the plastic shearing on slip systems. Here for a BCC crystal, 12 {110} <111> slip systems are considered (Cereceda et al., 2016; Stukowski et al., 2015). Therefore, \mathbf{L}^p is expressed as

$$\mathbf{L}^p = \sum_{\chi=1}^{12} \dot{\gamma}^\chi \mathbf{m}_\chi \otimes \mathbf{n}_\chi,$$

where $\dot{\gamma}^\chi$ is the plastic strain rate on the χ -th slip system, \mathbf{m}_χ and \mathbf{n}_χ are the unit vectors of the normal and shear directions of the χ -th slip system.

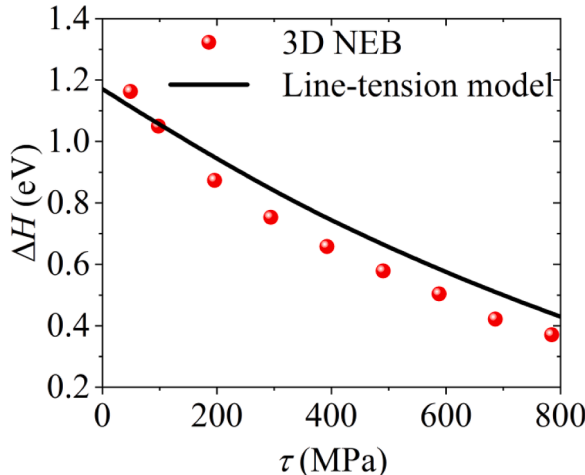


Fig. 13. Comparison between predictions from the stochastic line tension model and 3D NEB simulation results.

Considering long-distance athermal resistances, such as forest dislocation strengthening (Fan et al., 2021) and Hall–Petch effect in polycrystals (Han and Yi, 2021; Liu et al., 2020), the plastic strain rate on specific slip systems is described by a power law (Hill and Rice, 1972; Terentyev et al., 2015)

$$\dot{\gamma}^\chi = \dot{\gamma}_0 \left(\frac{|\tau_{\text{RSS}}^\chi|}{\tau_{\text{CRSS}}^\chi} \right)^{\frac{1}{m}} \text{sgn}(\tau_{\text{RSS}}^\chi), \quad (16)$$

where $\dot{\gamma}^\chi$ is the plastic strain rate of the χ -th slip system, τ_{RSS}^χ is the resolved shear stress of the χ -th slip system, m is the strain rate sensitive factor and $\text{sgn}(\tau_{\text{RSS}}^\chi)$ denotes the sign of τ_{RSS}^χ . The critical resolved shear stress (CRSS) τ_{CRSS}^χ is given as (Liu et al., 2023; Terentyev et al., 2015; Xiao et al., 2015)

$$\tau_{\text{CRSS}}^\chi(T) = \tau_f + \tau_{\text{HP}} + \tau_{\text{th}}, \quad (17)$$

where τ_f is the resistance from the forest dislocations, τ_{HP} is the strengthening from grain boundaries, and τ_{th} is the thermal resistance from the lattice friction. τ_f is given by $\tau_f = \alpha \mu b \sqrt{\rho}$ where α denotes the hardening coefficient of forest dislocation, μ is the shear modulus, ρ is the initial dislocation density. τ_{HP} is given by $\tau_{\text{HP}} = k_{\text{HP}} / \sqrt{d}$, where k_{HP} is a Hall–Petch parameter (Han and Yi, 2021; Liu et al., 2020), and d is the gain size. The temperature contribution to the forest dislocation resistance τ_f is neglected, as τ_f tends to change slowly with temperature, mainly caused by the change in elastic modulus μ . The strain hardening is given as (Mecking and Kocks, 1981)

$$\dot{\rho}^\chi = |\dot{\gamma}^\chi|(k_1 \rho^\chi - k_2 \rho^\chi) \quad (18)$$

where k_1 and k_2 are dislocation multiplication and annihilation parameters, respectively.

Here, we assume that the thermal part of the resistance τ_{th} is controlled by the predominant resistance between the contribution from screw dislocations and edge dislocations, since the macroscopic plastic flow requires the collective motion of these two types of dislocations. In a word, τ_{th} is taken to be the larger one of τ_s and τ_e . The determination of τ_s and τ_e is described as follows.

For screw dislocations, the activation barrier $\Delta H_s(\tau)$ can be obtained from the 3D NEB simulations in Section 2. After applying the averaging process in Section 2.2 to the 3D NEB simulation results, the resulting data of activation barrier is fitted to the Kocks form: $\Delta H_s(\tau) = \Delta H_{s0}[1 - (\tau/\tau_{s0})^{p_s}]^{q_s}$, where ΔH_{s0} , τ_{s0} , p_s and q_s are parameters from atomistic simulations with their values listed in Table 1. The physical meaning of ΔH_{s0} is the activation barrier for kink-pair nucleation when the shear stress is zero, τ_{s0} is the slip resistance at 0 K. According to transition state theory (Vineyard, 1957), the plastic strain rate $\dot{\gamma}$ is related to the activation barrier by $\dot{\gamma} = \dot{\gamma}_0 \exp[-\Delta H(\tau)/k_B T]$, where $\dot{\gamma}_0$ is the reference strain rate and $\Delta H(\tau)$ is the activation barrier as a function of shear stress. Therefore, the temperature-dependent stress originating from the screw dislocation kink-pair nucleation is

$$\tau_s = \tau_{s0} \left[1 - \left(\frac{kT}{\Delta H_{s0}} \ln \frac{\dot{\gamma}_{s0}}{\dot{\gamma}} \right)^{\frac{1}{p_s}} \right]^{\frac{1}{q_s}}, \quad (19)$$

where the reference plastic strain rate $\dot{\gamma}_{s0}$ is taken to be $3.17 \times 10^7 \text{ s}^{-1}$ (Narayanan et al., 2014). Similarly, the resistance attributed to edge dislocation motion is

$$\tau_e = \tau_{e0} \left[1 - \left(\frac{kT}{\Delta H_{e0}} \ln \frac{\dot{\gamma}_{e0}}{\dot{\gamma}} \right)^{\frac{1}{p_e}} \right]^{\frac{1}{q_e}}, \quad (20)$$

where $p_e = 1$ and $q_e = 1.5$, supposing a sinusoidal activation barrier (Maresca and Curtin, 2020). The athermal flow stress τ_{e0} and activation barrier ΔH_{e0} are obtained using the solid solution strengthening theory as (Maresca and Curtin, 2020)

$$\tau_{e0} = 0.040 \eta^{\frac{1}{3}} \bar{\mu} \left(\frac{1 + \bar{v}}{1 - \bar{v}} \right)^{\frac{4}{3}} \frac{\left(\sum_n c_n \Delta V_n^2 \right)^{\frac{2}{3}}}{b^4}, \quad (21)$$

$$\Delta H_{e0} = 2.00 \eta^{\frac{1}{3}} \bar{\mu} b \left(\frac{1 + \bar{v}}{1 - \bar{v}} \right)^{\frac{2}{3}} \left(\sum_n c_n \Delta V_n^2 \right)^{\frac{1}{3}}. \quad (22)$$

The line tension parameter η is taken as a fitting parameter here, and other variables in Eqs. (21) and (22) are taken from the atomic simulations in Maresca and Curtin (2020).

Table 1
Atomistically-determined parameters for stress-dependent activation barrier.

ΔH_{s0}	τ_{s0}	p_s	q_s
1.42 eV	1.50 GPa	0.40	1.00

We perform crystal plasticity simulations of uniaxial compression of NbMoTaW by incorporating the equations above into ABAQUS/Explicit as a user material subroutine VUMAT. The polycrystal model of NbMoTaW is taken as an assembly of 8000 grains with random orientations, each grain represented by an element with reduced integration (C3D8R). The strain rate sensitive factor m is 0.05 (Hill and Rice, 1972; Terentyev et al., 2015). The grain size d is set at $200\text{ }\mu\text{m}$ (Senkov et al., 2011) and the initial dislocation density ρ is $1 \times 10^{13}\text{ m}^{-2}$ (Argon, 2008). The line-tension parameter η is 0.5. The temperature dependence of the single crystal elastic constants are determined by measuring the change in the average stress tensor in an NVT simulations when the supercell undergoes finite deformation (Zhen and Chu, 2012). At 0 K, C_{11} , C_{12} and C_{44} are respectively 345 GPa, 143 GPa and 73 GPa, which align with the DFT results (Maresca and Curtin, 2020). Also, C_{11} decreases with increasing temperature, while C_{12} and C_{44} vary little with temperature. C_{11} is fitted using a quadratic function (Lowrie and Gonias, 1967) to be $C_{11}=342.28 + 6.99 \times 10^{-2}T - 2.23 \times 10^{-5}T^2$. Other parameters are shown in Table 2.

The predicted strain-stress relationships of NbMoTaW at 296 K and 873 K are shown in Fig. 14(a). The simulation results match well with experimental data (Senkov et al., 2011), though the stress drop due to the ambient temperature brittleness is not captured by our model. Fig. 14(b) shows the predicted yield strength. In the low-temperature region, the effect of screw dislocation is prominent, and the yield stress diminishes rapidly with increasing temperature due to the small activation volume of kink-pair nucleation, on the order of several b^3 . This indicates that the ambient temperature yield strength of NbMoTaW can be well predicted by the kink-pair nucleation mechanism of screw dislocations, while strengthening originating from screw dislocations does not predominate at high temperatures. Above 400 K, the yield strength is controlled by edge dislocations, changing slowly with temperature. The solid solution strengthening theory, as represented by Eqs. (21) and (22), predicts a large activation volume of edge dislocation glide. The larger activation volume of edge dislocation glide than that of screw dislocations is in line with the nano-pinning mechanism reported by Chen et al. (2020a), since the activation volume of nano-pinning is on the order of lb^2 , where l is the distance between pinning points and is much larger than b . However, the consideration of screw dislocation provides valuable insights into the lower-temperature behavior of BCC HEAs, and our methodology establishes a solid foundation for the atomistic determination of effective dislocation behavior in random solution solids.

5. Discussions

5.1. Statistical analysis

Our NEB simulations reveal that screw dislocation motion in HEAs follows a two-step process: kink-pair nucleation and kink migration. Kink-pair nucleation is the rate-limiting process in pure BCC metals. In dilute BCC alloys, kink-pair nucleation is still the rate-limiting process, albeit with a reported softening effect due to energy landscape fluctuations (Ghafarollahi and Curtin, 2020). These fluctuations may create more favorable locations, or “weakest links”, for kink-pair nucleation (Ghafarollahi and Curtin, 2020). However, without cross-slip, a relatively straight screw dislocation must pass all Peierls hills in succession to induce plastic flow. As a result, the “strongest link” can be rate-limiting along the forward direction, as shown by the relationship between the dislocation profile and the pinning point landscape (Utt et al., 2022). To account for both mechanisms, we propose a two-level averaging method. Our method is supported by phase field dislocation dynamics simulations of screw dislocation in RHEAs (Fey et al., 2022), which demonstrates that the critical stress to initiate dislocation motion depends on the weakest region, and to maintain the motion over more Peierls barriers, the critical stress can increase.

5.2. The effect of cross-slip

In BCC metals, cross slip is easy and the motion of screw dislocation can thus become three-dimensional. While this phenomenon may also occur in RHEAs, few studies have focused on this aspect. Two opposite effects can result from the cross slip of screw dislocations. On the one hand, shifting to other slip planes may offer a way to overcome strong barriers and soften the RHEAs. On the other hand, cross-slip on different slip planes can lead to a self-pinning phenomenon called cross-kink, which has a strengthening effect. It is important to note that we have not considered the cross-slip mechanism in the present work. The cross-kink strengthening has been observed in RHEAs (Eleti et al., 2022; Zhou et al., 2021), which may extend the dominance of screw dislocation to higher-temperature regions. A detailed study of this effect using the NEB method (Wang and Cai, 2023) will be addressed in our future work.

5.3. The effect of edge dislocation

We adopt a theoretical model (Eqs. (21) and (22)) to describe the solid solution strengthening of edge dislocations (Maresca and Curtin, 2020). However, this model struggles to reproduce the high-strength “plateau”, as it only considers the average elastic interaction energy of solutes in the dislocation displacement field (Maresca and Curtin, 2020). As observed in previous atomic simulations (Kubilay et al., 2021), edge dislocations can also be locally pinned by certain clusters and can be unpinned by a bow-out process. The bow-out process may lead to an even larger activation volume and may partly account for the slow change of strength at moderate temperatures, which is worthy of future investigation.

Table 2

Material parameters for the crystal plasticity model.

k_1	k_2	α	k_{HP}
$4.10 \times 10^8 \text{ m}^{-1}$	0.70	0.50	$0.45 \text{ MPa m}^{1/2}$

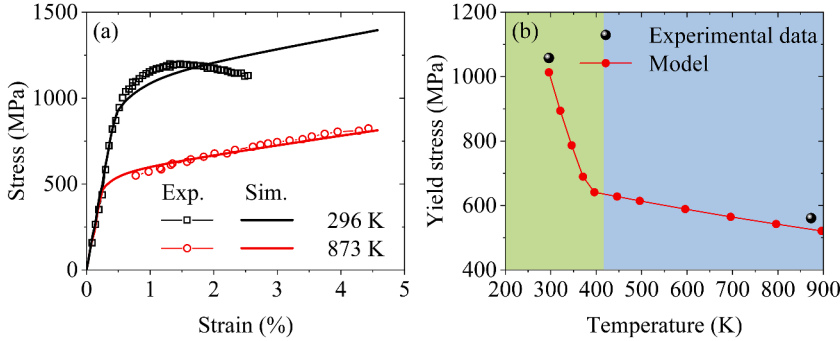


Fig. 14. (a) Present theoretical predictions alongside experimental stress-strain curves of NbMoTaW at different temperatures (Senkov et al., 2011). (b) Present theoretical predictions and experimental data of the temperature-dependent yield stress for NbMoTaW alloy (Senkov et al., 2011). Green and blue region denotes the dominance of screw and edge dislocation, respectively.

6. Conclusions

In this study, we have conducted systematic 3D NEB simulations on screw dislocations and performed statistical analysis on the resulting data. Additionally, we have established a stochastic line tension model to offer a theoretical perspective on kink-pair nucleation energy. Moreover, a multiscale simulation framework is established to analyze the uniaxial loading response of RHEAs at various temperatures. The main conclusions are outlined below.

- The statistical analysis of NEB simulation results shows a two-region distribution, highlighting two distinct mechanisms of screw dislocation glide: kink-pair nucleation and kink migration. Activation barrier of kink-pair nucleation is statistically higher than that of kink migration, suggesting that kink-pair nucleation is the rate-limiting process of screw dislocation glide in NbMoTaW, as is the case in pure BCC metals.
- An averaging method is developed to determine the effective activation barrier of kink-pair nucleation. This method involves identifying the weakest link along a dislocation length and incorporating it into the waiting-time averaging, yielding a two-level averaging approach that aligns closely with the physical interpretation.
- A direct relationship between the activation barrier and the initial-final enthalpy difference, involving both the kink-pair nucleation barrier from 3D NEB simulations and Peierls barrier from 2D NEB simulations, is identified.
- A line tension model, assigning a stochastic Peierls barrier to each dislocation segment, is proposed. The model prediction for kink-pair nucleation energy agrees well with 3D NEB simulations, offering a substantial reduction in computational cost.
- Using the enthalpy-stress function obtained from atomistic simulation, we have established an atomistically-informed crystal plasticity framework, facilitating accurate determination of the yield strength and stress-strain response of RHEAs. Our methodology provides a solid foundation for determining the effective dislocation behavior in random solution alloys at the atomistic level.

CRediT authorship contribution statement

Feng Zhao: Conceptualization, Methodology, Software, Validation, Formal analysis, Writing – original draft. **Wenbin Liu:** Methodology, Writing – review & editing. **Xin Yi:** Investigation, Writing – review & editing. **Yin Zhang:** Investigation, Software, Writing – review & editing. **Huiling Duan:** Writing – review & editing, Supervision, Project administration, Funding acquisition.

Declaration of competing interest

The authors declare that they have no known competing financial interests or personal relationships that could have appeared to influence the work reported in this paper.

Acknowledgments

H. D. acknowledge the financial support provided by the National Natural Science Foundation of China (grant No. 11988102). Y.Z. acknowledge the financial support provided by the Fundamental Research Funds for the Central Universities, Peking University. The

authors gratefully acknowledge the computing resources provided by the High-performance Computing Platform of Peking University and the Sugon Computing Center in Xi'an.

References

- Argon, A., 2008. Strengthening Mechanisms in Crystal Plasticity. Oxford University Press Inc., New York.
- Cereceda, D., Diehl, M., Roters, F., Raabe, D., Perlado, J.M., Marian, J., 2016. Unraveling the temperature dependence of the yield strength in single-crystal tungsten using atomistically-informed crystal plasticity calculations. *Int. J. Plast.* 78, 242–265.
- Chaussidon, J., Fivel, M., Rodney, D., 2006. The glide of screw dislocations in bcc Fe: atomistic static and dynamic simulations. *Acta Mater.* 54, 3407–3416.
- Chen, B., Li, S., Ding, J., Ding, X., Sun, J., Ma, E., 2023. Correlating dislocation mobility with local lattice distortion in refractory multi-principal element alloys. *Scr. Mater.* 222, 115048.
- Chen, B., Li, S., Zong, H., Ding, X., Sun, J., Ma, E., 2020a. Unusual activated processes controlling dislocation motion in body-centered-cubic high-entropy alloys. *Proc. Natl. Acad. Sci. U.S.A.* 117, 16199–16206.
- Chen, L., Liu, W., Yu, L., Cheng, Y., Ren, K., Sui, H., Yi, X., Duan, H., 2020b. Probabilistic and constitutive models for ductile-to-brittle transition in steels: a competition between cleavage and ductile fracture. *J. Mech. Phys. Solids* 135, 103809.
- Coury, F.G., Kaufman, M., Clarke, A.J., 2019. Solid-solution strengthening in refractory high entropy alloys. *Acta Mater.* 175, 66–81.
- Dezerald, L., Provost, L., Ventelon, L., Willaime, F., Rodney, D., 2015. First-principles prediction of kink-pair activation enthalpy on screw dislocations in bcc transition metals: V, Nb, Ta, Mo, W, and Fe. *Phys. Rev. B* 91, 094105.
- Ding, Q., Zhang, Y., Chen, X., Fu, X., Chen, D., Chen, S., Gu, L., Wei, F., Bei, H., Gao, Y., Wen, M., Li, J., Zhang, Z., Zhu, T., Ritchie, R.O., Yu, Q., 2019. Tuning element distribution, structure and properties by composition in high-entropy alloys. *Nature* 574, 223–227.
- Eleti, R.R., Stepanov, N., Yurchenko, N., Zherebtsov, S., Maresca, F., 2022. Cross-kink unpinning controls the medium- to high-temperature strength of body-centered cubic NbTiZr medium-entropy alloy. *Scr. Mater.* 209, 114367.
- Fan, H., Wang, Q., El-Awady, J.A., Raabe, D., Zaiser, M., 2021. Strain rate dependency of dislocation plasticity. *Nat. Commun.* 12, 1845.
- Fan, Y., Ossetskiy, Y.N., Yip, S., Yıldız, B., 2013. Mapping strain rate dependence of dislocation-defect interactions by atomistic simulations. *Proc. Natl. Acad. Sci. U.S.A.* 110, 17756–17761.
- Fang, Q., Lu, W., Chen, Y., Feng, H., Liaw, P.K., Li, J., 2022. Hierarchical multiscale crystal plasticity framework for plasticity and strain hardening of multi-principal element alloys. *J. Mech. Phys. Solids* 169, 105067.
- Fey, L.T.W., Xu, S., Su, Y., Hunter, A., Beyerlein, I.J., 2022. Transitions in the morphology and critical stresses of gliding dislocations in multiprincipal element alloys. *Phys. Rev. Mater.* 6, 013605.
- George, E.P., Raabe, D., Ritchie, R.O., 2019. High-entropy alloys. *Nat. Rev. Mater.* 4, 515–534.
- Ghafarollahi, A., Curtin, W.A., 2020. Theory of double-kink nucleation in dilute BCC alloys. *Acta Mater.* 196, 635–650.
- Gurrutxaga-Lerma, B., Verschueren, J., Sutton, A.P., Dini, D., 2020. The mechanics and physics of high-speed dislocations: a critical review. *Int. Mater. Rev.* 66, 215–255.
- Han, Q., Yi, X., 2021. A unified mechanistic model for Hall-Petch and inverse Hall-Petch relations of nanocrystalline metals based on intragranular dislocation storage. *J. Mech. Phys. Solids* 154, 104530.
- He, S., Zhou, X., Mordehai, D., Marian, J., 2023. Thermal super-jogs control the high-temperature strength plateau in Nb-Mo-Ta-W alloys. *Acta Mater.* 244, 118539.
- Hill, R., Rice, J.R., 1972. Constitutive analysis of elastic-plastic crystals at arbitrary strain. *J. Mech. Phys. Solids* 20, 401–413.
- Hu, Y.J., Sundar, A., Ogata, S., Qi, L., 2021. Screening of generalized stacking fault energies, surface energies and intrinsic ductile potency of refractory multicomponent alloys. *Acta Mater.* 210, 116800.
- Hu, Y.J., Zhao, G., Zhang, B., Yang, C., Zhang, M., Liu, Z.K., Qian, X., Qi, L., 2019. Local electronic descriptors for solute-defect interactions in bcc refractory metals. *Nat. Commun.* 10, 4484.
- Kalidindi, S.R., Bronkhorst, C.A., Anand, L., 1992. Crystallographic texture evolution in bulk deformation processing of FCC metals. *J. Mech. Phys. Solids* 40, 537–569.
- Kang, K., Bulatov, V.V., Cai, W., 2012. Singular orientations and faceted motion of dislocations in body-centered cubic crystals. *Proc. Natl. Acad. Sci. u S. a* 109, 15174–15178.
- Kelchner, C.L., Plimpton, S., Hamilton, J., 1998. Dislocation nucleation and defect structure during surface indentation. *Phys. Rev. B* 58, 11085.
- Kotz, S., Nadarajah, S., 2000. Extreme Value Distributions: Theory and Applications. Imperial College Press, London.
- Kubilay, R.E., Ghafarollahi, A., Maresca, F., Curtin, W.A., 2021. High energy barriers for edge dislocation motion in body-centered cubic high entropy alloys. *npj Compt. Mater.* 7, 112.
- Kumar, P., Ludhwani, M.M., Das, S., Gavini, V., Kanjrala, A., Adlakha, I., 2023. Effect of hydrogen on plasticity of α -Fe: a multi-scale assessment. *Int. J. Plast.* 165, 103613.
- Labusch, R., 1988. Cooperative effects in alloy hardening. *Czech. J. Phys.* 38, 474–481.
- Lee, C., Kim, G., Chou, Y., Musico, B.L., Gao, M.C., An, K., Song, G., Chou, Y.C., Keppens, V., Chen, W., Liaw, P.K., 2020. Temperature dependence of elastic and plastic deformation behavior of a refractory high-entropy alloy. *Sci. Adv.* 6, eaaz4748.
- Lee, C., Maresca, F., Feng, R., Chou, Y., Ungar, T., Widom, M., An, K., Poplawsky, J.D., Chou, Y.C., Liaw, P.K., Curtin, W.A., 2021. Strength can be controlled by edge dislocations in refractory high-entropy alloys. *Nat. Commun.* 12, 5474.
- Li, W., Xie, D., Li, D., Zhang, Y., Gao, Y., Liaw, P.K., 2021. Mechanical behavior of high-entropy alloys. *Prog. Mater. Sci.* 118, 100777.
- Li, X.G., Chen, C., Zheng, H., Zuo, Y., Ong, S.P., 2020a. Complex strengthening mechanisms in the NbMoTaW multi-principal element alloy. *npj Compt. Mater.* 6, 70.
- Li, X., Li, W., Irving, D.L., Varga, L.K., Vitos, L., Schönecker, S., 2020b. Ductile and brittle crack-tip response in equimolar refractory high-entropy alloys. *Acta Mater.* 189, 174–187.
- Li, Z., Zhao, S., Ritchie, R.O., Meyers, M.A., 2019. Mechanical properties of high-entropy alloys with emphasis on face-centered cubic alloys. *Prog. Mater. Sci.* 102, 296–345.
- Lin, P., Nie, J., Liu, M., 2022. Multiscale crystal plasticity finite element model for investigating the irradiation hardening and defect evolution mechanism of A508-3 steel. *Nucl. Mater. Energy* 32, 101214.
- Liu, W., Liu, Y., Cheng, Y., Chen, L., Yu, L., Yi, X., Duan, H., 2020. Unified model for size-dependent to size-independent transition in yield strength of crystalline metallic materials. *Phys. Rev. Lett.* 124, 235501.
- Liu, W., Zhao, F., Yu, L., Cheng, Y., Duan, H., 2023. A constitutive framework for micro-to-macroplasticity of crystalline materials under monotonic and cyclic deformation. *J. Mech. Phys. Solids* 179, 105383.
- Lowrie, R., Gonias, A.M., 1967. Single-crystal elastic properties of tungsten from 24° to 1800°C . *J. Appl. Phys.* 38, 4505–4509.
- Mak, E., Yin, B., Curtin, W.A., 2021. A ductility criterion for bcc high entropy alloys. *J. Mech. Phys. Solids* 152, 104389.
- Maresca, F., Curtin, W.A., 2020. Mechanistic origin of high strength in refractory BCC high entropy alloys up to 1900K. *Acta Mater.* 182, 235–249.
- Mecking, H., Koocks, U.F., 1981. Kinetics of flow and strain-hardening. *Acta Metall.* 29, 1865–1875.
- Narayanan, S., McDowell, D.L., Zhu, T., 2014. Crystal plasticity model for BCC iron atomistically informed by kinetics of correlated kinkpair nucleation on screw dislocation. *J. Mech. Phys. Solids* 65, 54–68.
- Nöhring, W.G., Curtin, W.A., 2017. Dislocation cross-slip in fcc solid solution alloys. *Acta Mater.* 128, 135–148.
- Phillips, R., 2001. Crystals, defects and microstructures: modeling across scales. Cambridge University Press, Cambridge, UK.
- Po, G., Cui, Y., Rivera, D., Cereceda, D., Swinburne, T.D., Marian, J., Ghoniem, N., 2016. A phenomenological dislocation mobility law for bcc metals. *Acta Mater.* 119, 123–135.

- Qi, L., Chrzan, D.C., 2014. Tuning ideal tensile strengths and intrinsic ductility of bcc refractory alloys. *Phys. Rev. Lett.* 112, 115503.
- Rodney, D., Provost, L., 2009. Stress-dependent Peierls potential: influence on kink-pair activation. *Phys. Rev. B* 79, 094108.
- Rodney, D., Ventelon, L., Clouet, E., Pizzagalli, L., Willaime, F., 2017. Ab initio modeling of dislocation core properties in metals and semiconductors. *Acta Mater.* 124, 633–659.
- Seeger, A., 1995. The flow stress of high-purity refractory body-centred cubic metals and its modification by atomic defects. *Le J. de Phys. IV* 5, 45–65.
- Seeger, A., 2001. Why anomalous slip in body-centred cubic metals? *Mater. Sci. Eng. A* 319, 254–260.
- Seeger, A., Holzwarth, U., 2006. Slip planes and kink properties of screw dislocations in high-purity niobium. *Philos. Mag.* 86, 3861–3892.
- Senkov, O., Wilks, G., Miracle, D., Chuang, C., Liaw, P., 2010. Refractory high-entropy alloys. *Intermetallics (Barking)* 18, 1758–1765.
- Senkov, O.N., Miracle, D.B., Chaput, K.J., Couzinie, J.P., 2018. Development and exploration of refractory high entropy alloys—A review. *J. Mater. Res.* 33, 3092–3128.
- Senkov, O.N., Miracle, D.B., Rao, S.I., 2021. Correlations to improve room temperature ductility of refractory complex concentrated alloys. *Mater. Sci. Eng. A* 820, 141512.
- Senkov, O.N., Wilks, G.B., Scott, J.M., Miracle, D.B., 2011. Mechanical properties of Nb25Mo25Ta25W25 and V20Nb20Mo20Ta20W20 refractory high entropy alloys. *Intermetallics (Barking)* 19, 698–706.
- Shimizu, F., Ogata, S., Kimizuka, H., Kano, T., Li, J., Kaburaki, H., 2007. First-principles calculation on screw dislocation core properties in BCC molybdenum. *J. Earth Simulator* 7, 17–21.
- Si, Y., Zhang, Y., Chen, D., Wormald, J.L., Anglin, B.S., McDowell, D.L., Zhu, T., 2023. Atomistic determination of Peierls barriers of dislocation glide in nickel. *J. Mech. Phys. Solids* 178, 105359.
- Stukowski, A., 2010. Visualization and analysis of atomistic simulation data with OVITO—the open visualization tool. *Modelling Simul. Mater. Sci. Eng.* 18, 015012.
- Stukowski, A., Cereceda, D., Swinburne, T.D., Marian, J., 2015. Thermally-activated non-Schmid glide of screw dislocations in W using atomistically-informed kinetic Monte Carlo simulations. *Int. J. Plast.* 65, 108–130.
- Tandoc, C., Hu, Y.J., Qi, L., Liaw, P.K., 2023. Mining of lattice distortion, strength, and intrinsic ductility of refractory high entropy alloys. *npj Compt. Mater.* 9, 53.
- Terentyev, D., Xiao, X., Dubinko, A., Bakaeva, A., Duan, H., 2015. Dislocation-mediated strain hardening in tungsten: thermo-mechanical plasticity theory and experimental validation. *J. Mech. Phys. Solids* 85, 1–15.
- Thompson, A.P., Aktulga, H.M., Berger, R., Bolintineanu, D.S., Brown, W.M., Crozier, P.S., in 't Veld, P.J., Kohlmeyer, A., Moore, S.G., Nguyen, T.D., Shan, R., Stevens, M.J., Tranchida, J., Trott, C., Plimpton, S.J., 2022. LAMMPS - a flexible simulation tool for particle-based materials modeling at the atomic, meso, and continuum scales. *Comp. Phys. Commun.* 271, 108171.
- Tsai, M.H., Yeh, J.W., 2014. High-entropy alloys: a critical review. *Mater. Res. Lett.* 2, 107–123.
- Utt, D., Lee, S., Xing, Y., Jeong, H., Stukowski, A., Oh, S.H., Dehm, G., Albe, K., 2022. The origin of jerky dislocation motion in high-entropy alloys. *Nat. Commun.* 13, 4777.
- Vineyard, G.H., 1957. Frequency factors and isotope effects in solid state rate processes. *J. Phys. Chem. Solids* 3, 121–127.
- Vitek, V., Perrin, R.C., Bowen, D.K., 1970. The core structure of $\frac{1}{2}(111)$ screw dislocations in b.c.c. crystals. *Philos. Mag.* 21, 1049–1073.
- Wang, F., Balbus, G.H., Xu, S., Su, Y., Shin, J., Rottmann, P.F., Knipling, K.E., Stinville, J.C., Mills, L.H., Senkov, O.N., Beyerlein, I.J., Pollock, T.M., Gianola, D.S., 2020. Multiplicity of dislocation pathways in a refractory multiprincipal element alloy. *Science (1979)* 370, 95–101.
- Wang, X., Maresca, F., Cao, P., 2022. The hierarchical energy landscape of screw dislocation motion in refractory high-entropy alloys. *Acta Mater.* 234, 118022.
- Wang, X., Xu, S., Jian, W.R., Li, X.G., Su, Y., Beyerlein, I.J., 2021. Generalized stacking fault energies and Peierls stresses in refractory body-centered cubic metals from machine learning-based interatomic potentials. *Comp. Mater. Sci.* 192, 110364.
- Wang, Y., Cai, W., 2023. Stress-dependent activation entropy in thermally activated cross-slip of dislocations. *Proc. Natl. Acad. Sci. U.S.A.* 120, e2222039120.
- Weibull, W., 1939. The phenomenon of rupture in solids. *Proc. R. Swedish Inst. Eng. Res.* 153, 1–55.
- Xiao, X., Song, D., Xue, J., Chu, H., Duan, H., 2015. A self-consistent plasticity theory for modeling the thermo-mechanical properties of irradiated FCC metallic polycrystals. *J. Mech. Phys. Solids* 78, 1–16.
- Xiong, W., Guo, A.X.Y., Zhan, S., Liu, C.T., Cao, S.C., 2023. Refractory high-entropy alloys: a focused review of preparation methods and properties. *J. Mater. Sci. Tech.* 142, 196–215.
- Yin, S., Zuo, Y., Abu-Odeh, A., Zheng, H., Li, X.G., Ding, J., Ong, S.P., Asta, M., Ritchie, R.O., 2021. Atomistic simulations of dislocation mobility in refractory high-entropy alloys and the effect of chemical short-range order. *Nat. Commun.* 12, 4873.
- Zhang, C., Wang, H., Wang, X., Tang, Y.T., Yu, Q., Zhu, C., Xu, M., Zhao, S., Kou, R., Wang, X., MacDonald, B.E., Reed, R.C., Vecchio, K.S., Cao, P., Rupert, T.J., Lavernia, E.J., 2023. Strong and ductile refractory high-entropy alloys with super formability. *Acta Mater.* 245, 118602.
- Zhang, Y., Ding, K., Stangeby, S., Chen, D., Kacher, J., Pierron, O., Zhu, T., 2022. Atomistic modeling of surface and grain boundary dislocation nucleation in FCC metals. *Acta Mater.* 237, 118155.
- Zhang, Y., Zuo, T.T., Tang, Z., Gao, M.C., Dahmen, K.A., Liaw, P.K., Lu, Z.P., 2014. Microstructures and properties of high-entropy alloys. *Prog. Mater. Sci.* 61, 1–93.
- Zhen, Y., Chu, C., 2012. A deformation-fluctuation hybrid method for fast evaluation of elastic constants with many-body potentials. *Comp. Phys. Commun.* 183, 261–265.
- Zheng, H., Fey, L.T.W., Li, X.G., Hu, Y.J., Qi, L., Chen, C., Xu, S., Beyerlein, I.J., Ong, S.P., 2023. Multi-scale investigation of short-range order and dislocation glide in MoNbTi and TaNbTi multi-principal element alloys. *npj Compt. Mater.* 9, 89.
- Zhou, X., He, S., Marian, J., 2021. Cross-kinks control screw dislocation strength in equiatomic bcc refractory alloys. *Acta Mater.* 211, 116875.
- Zhou, X., Wang, X., Fey, L., He, S., Beyerlein, I., Cao, P., Marian, J., 2023. Models of dislocation glide and strengthening mechanisms in bcc complex concentrated alloys. *MRS Bull.* 48, 777–789.
- Zhu, T., Li, J., Yip, S., 2013. Atomistic reaction pathway sampling: the nudged elastic band method and nanomechanics applications. *Nano and Cell Mechanics: Fundamentals and Frontiers*. John Wiley & Sons, Ltd, pp. 311–338.